



Pupil apodization in digital holographic microscopy for reduction of coherent imaging effects

CHRISTOS MESSINIS,^{1,2,*}  MANASHEE ADHIKARY,^{1,2} 
TAMAR CROMWIJK,^{1,2} THEODORUS T. M. VAN SCHAIJK,³ 
STEFAN WITTE,^{1,2}  JOHANNES F. DE BOER,¹ 
AND ARIE DEN BOEF^{1,2,3}

¹*Department of Physics and Astronomy, and LaserLaB, Vrije Universiteit, De Boelelaan 1081, 1081 HV Amsterdam, The Netherlands*

²*Advanced Research Center for Nanolithography (ARCNL), Science Park 106, 1098 XG Amsterdam, The Netherlands*

³*ASML Netherlands B.V., De Run 6501, 5504 DR, Veldhoven, The Netherlands*

**c.messinis@arcnl.nl*

Abstract: A dark-field Digital Holographic Microscope with a single lens for imaging is a potential candidate for future overlay metrology on semiconductor wafers. Aberrations caused by this single lens are computationally corrected allowing high-resolution imaging over a large wavelength range. However, the spatially-coherent imaging conditions in our microscope introduce coherent imaging artifacts that can limit the metrology performance. We present computational apodization of the optical field in the exit pupil of the lens as a potentially effective solution to mitigate these coherent imaging effects. A comparison of experimental data and simulations is presented that demonstrates the importance of this apodization in metrology applications. Moreover, our data also shows that exploiting the full potential of DHM requires an imaging lens with low optical scattering levels.

© 2022 Optica Publishing Group under the terms of the [Optica Open Access Publishing Agreement](#)

1. Introduction

Digital Holographic Microscopy (DHM) is a well-known and established technique for high resolution imaging in various application domains like bio-medical imaging and semiconductor defect inspection [1–4]. DHM acquires the amplitude and phase of an image which offers various unique opportunities like (3D) imaging of low-contrast objects and digital aberration correction [5,6]. Recently we have reported the use of dark-field DHM (df-DHM) as a potential solution for the growing challenges of overlay (OV) metrology in semiconductor industry [7,8].

In semiconductor device manufacturing the relative placement between various patterned layers in a chip (called Overlay) must be robustly measured with sub-nanometer precision. This measurement can, for example, be done with a technique called Diffraction Based Overlay (DBO) [9]. In DBO a pair of small overlapping gratings is illuminated resulting in the generation of a +1st and a -1st diffraction order. An overlay error between these overlapping gratings creates a small intensity difference between these orders, which scales linearly with overlay. Today, high-resolution dark-field microscopy is commonly used to image the +1st and -1st diffraction order images of the metrology targets on a camera and these images are used to determine overlay. Robustness and sub-nm accuracy is possible by optimizing the grating etch and using carefully selected multiple wavelengths [10].

However, the relentless push to follow Moore's law [11] drives existing optical overlay metrology to the extreme limits of its capabilities. Novel devices and process flows result in the use of new materials (like amorphous carbon) that are highly absorbing at visible wavelengths

but sufficiently transparent at infrared wavelengths. This drives the need for metrology tools that can cover a larger wavelength range. In addition, there is a strong push to reduce the size of the metrology targets that requires improved imaging resolution. On top of this, the diffraction efficiency of metrology targets continues to decrease to unprecedented low levels due to thin resist that is used in (high-NA) EUV lithography and increased light losses in the stack of layers that cover the bottom grating. Last but not least, a solution for all these challenges needs to be realized at acceptable cost and in a small footprint since available space for metrology is limited.

A promising solution to all these challenges is dark-field Digital Holographic Microscopy (df-DHM). In a previous publication [7] we proposed the use of df-DHM that uses a tunable quasi-monochromatic spatially coherent light source. The use of 2 off-axis reference beams with different azimuthal angles allows angular frequency multiplexing, enabling the separate imaging of the $+1^{\text{st}}$ and -1^{st} diffraction orders using the full NA of the imaging lens which improves imaging resolution. A schematic drawing of df-DHM is shown in Fig. 1. The off-axis df-DHM setup uses a fiber coupled Supercontinuum White light source (Leukos Rock 400 5) combined with an Acousto-Optical Tunable Filter (Gooch & Housego TF550-300-4-6-GH57A). This AOTF device has a bandwidth in the range of 4–7 nm and covers the whole visible wavelength range from 400 to 700 nm. A delay line is used to match the optical path of the reference and the illumination beam and polarization maintaining fibers (PM - Shafter-Kirchhoff PMC-400Si-2.3-NA014) are used to couple the light from the source path to the sensor head. The sensor head is comprised of two off-axis illumination arms which illuminate the target from opposite directions at an incident angle of approximately 70° with respect to the normal of the object plane.

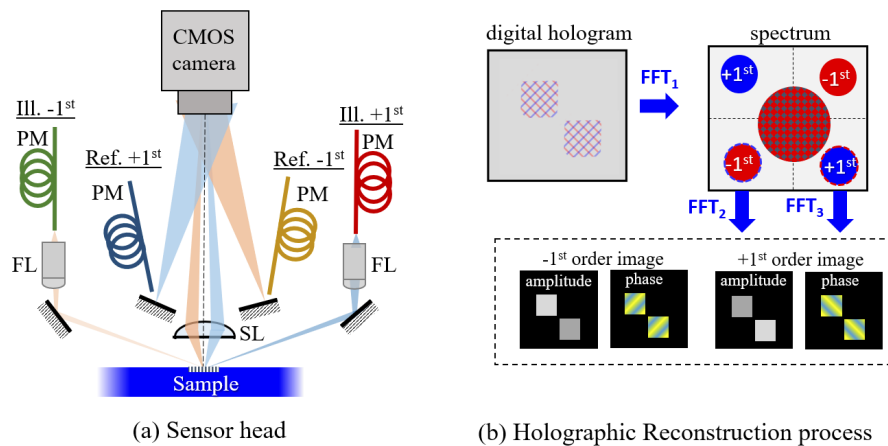


Fig. 1. (a) the fiber-coupled df-DHM. The sample is illuminated with two oblique illumination beams (Ill. $+1^{\text{st}}$ and Ill. -1^{st}) of $\pm 70^\circ$ respectively. The object beams are captured by the imaging lens (SL) and coherently mixed with their respective reference beams (Ref. $+1^{\text{st}}$ and Ref. -1^{st}) resulting in a hologram on image plane (CMOS camera). (b) the holographic reconstruction process. The camera image contains two interference patterns initially introduced by the two separate branches. By Fourier transforming the hologram we back-propagate to the pupil plane and the angular spectrum. The illumination branches have different azimuthal angles in the reference arms resulting in a 90° angle difference. For reconstruction of the complex field two Fast Fourier Transforms for the two interference terms are required.

For DBO measurements the two sides generate the -1^{st} (L. Arm) and $+1^{\text{st}}$ (R. Arm) diffraction orders. Each illumination arm generates a Gaussian-shaped spot on the object plane ($1/e^2$ diameter approximately $130\ \mu\text{m}$) with the use of two microscope objectives (FL- 50X Mitutoyo Plan Apo Infinity Corrected Long WD Objective) and two adjustable mirrors for fine-tuning the

angle of incidence. In addition, two corresponding spherical reference beams are coherently added to the corresponding object beams. The two reference beams have different azimuthal angles resulting in a different orientation of the sidebands of the spectra of the resulting holograms. With this approach, two holograms are captured by the image sensor using only one image acquisition, and the two object fields can be retrieved with only three Fast Fourier Transforms (FFTs). Further details of this setup and the parallel acquisition of multiple holograms are given in [7]. The microscope consists of a single plano-aspheric Thorlabs lens (SL) and a camera (Basler acA4112-8gm) with a 12 Mpixel CMOS image sensor with $3.45\ \mu\text{m}$ pixel size. We chose a nominal magnification of 100x by placing our detector 800 mm away from the lens.

It is worth mentioning that the coherent mixing of the diffracted orders with their respective reference beams offers noiseless optical amplification which lifts the image above the noise floor of the image sensor and boosts the detection sensitivity of very weak metrology targets. This has already been demonstrated in [8], where a weak measured signal of a silicon wafer at 1030 nm wavelength is coherently mixed with a reference beam resulting in a "noise clean" amplified holographic image. Finally, the retrieved complex field in DHM allows us to computationally correct for aberrations in the imaging lens [12]. A single imaging lens might seem undesired as it adds a quadratic wavefront to the complex image on the camera, but it is required as it enables imaging on a larger wavelength range. We eliminate this quadratic term by introducing a spherical reference beam that is propagated from the tip of a fiber placed in the pupil plane of the imaging lens.

However, our df-DHM concept operates in a spatially coherent imaging regime [13]. As a result, the Coherent Transfer Function of our df-DHM creates oscillatory edge transitions in the retrieved images (as shown in Fig. 2) that are undesired for metrology applications. In the next section we will briefly explain the impact of coherent imaging conditions in metrology applications, present digital pupil apodization as an effective solution and compare various implementations. Section 3 presents simulations and measurements on actual metrology targets along with point-spread functions (PSFs) for a better evaluation of the use of this method. Section 4 discusses the effectiveness of pupil apodization for metrology applications and the potential limitations and section 5 concludes the paper with an outline of the following steps that we plan to take to improve overlay metrology.

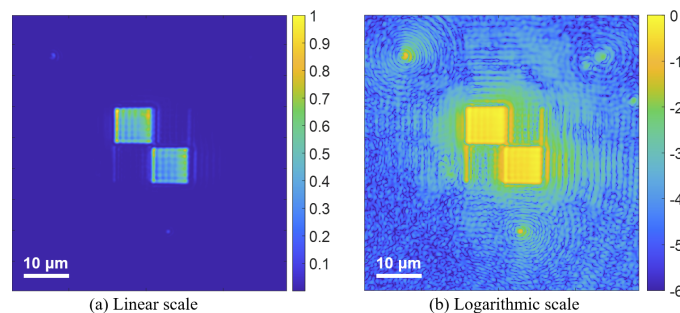


Fig. 2. Coherent imaging effects on our df-DHM. A metrology target's normalized intensity is imaged in (a) linear scale and (b) logarithmic scale.

2. Theory

2.1. Coherent imaging effects in DHM

We use DHM that requires a spatially coherent quasi-monochromatic illumination to enable interference between reference and object beam. This requirement also introduces inherent coherent imaging effects in the reconstructed images. In earlier work, the use of low spatial

coherent sources [14–16], multiplexing holograms methods [17–19], image processing methods [20,21], and hybrid methods [22,23] have been studied to improve the imaging quality. In our investigation, we look into a hybrid method of the use of a super continuum source combined with image processing method for coherent imaging effects reduction. But by definition, a super continuum source, even with low temporal coherence, introduces coherent effects to the holographic imaging, causing reduction of the sharpness of the reconstructed image and further degrading the imaging quality.

The coherent imaging effects that we can expect in our df-DHM will show up as:

1. Ringing effects at edges due to the steep cut-off of the Coherent Transfer Function
2. Increased optical crosstalk (X-talk) between neighboring patterns
3. Speckle (in case of rough surfaces)

In the numerical reconstruction of a hologram the commonly applied two-dimensional Discrete Fourier Transform (2D DFT) method on the pupil plane introduces Gibbs-ringing. This ringing effect is due to the presence of a sharp cut-off in the pupil plane that is forward-propagated to the image. Gibbs-ringing is a common artifact caused by the finite k-space sampling and is the effect of the truncation of higher frequencies at the sampling borders [24]. This shows up as spurious oscillations in the vicinity of high frequency region like the edges of a metrology target, as shown in Fig. 2. This phenomenon is more clearly present on the smallest metrology targets and remains even after aberration correction. As a result, these oscillations can degrade not only the quality of the images but also impact the metrology results obtained with df-DHM.

Gibbs-ringing is present mainly at the edges of a structure but it also expands in every direction. This means that the spurious oscillations can affect nearby structures also and result in additional coherent imaging effects with an overlap of high frequencies of different structure in k-space. This crosstalk should be minimized to allow precise metrology on targets that are surrounded by other patterns. This is an effect that becomes more visible for smaller metrology targets, and hence the higher frequencies are enlarged resulting in light leakage from one structure to a neighbouring structure.

Speckle is another undesired coherent imaging effect and it can generally be found in both reflection and transmission DHM. In reflection configuration, grain speckle occurs when the reflected light irradiates the sample surface. At the same time in both configurations non-diffusing objects can cause undesired diffraction, like dust particles, scratches, and defects on and in the optical components of the setup. Since our df-DHM concept is intended for high end semiconductor wafers we do not expect significant speckle noise originated from the wafer but we will show that in our df-DHM setup, weak scattering from the imaging lens can add a small amount of speckle to our measurements.

Figure 2 shows the coherent imaging effects that are currently present in our measured df-images. We selected a micro-DBO (μ DBO) metrology target with $8 \times 8 \mu\text{m}^2$ grating size that consists of four grating pairs with a grating pitch of 600 nm. Two of these grating pairs run in the vertical direction and are used to measure overlay in the horizontal direction, the other two grating pairs are used to measure overlay in the vertical direction but since we illuminate the sample from the horizontal direction they are not visible on a measured df-image. These grating pairs can potentially add coherent imaging effects in the measurements.

Figures 2(a) and 2(b) shows the presence of coherent effects on an aberration corrected dark-field intensity image in both linear and logarithmic scale. The selected wavelength for this measurement was 576 nm with a bandwidth of 5 nm. In more details, in linear scale we can already detect the spurious oscillations within the metrology marks. And in logarithmic scale it is revealed that ringing and cross talk from y grating marks are also affecting the metrology marks. Finally, some dust particles that are located around the targets increase the speckle noise on our measurements. This is mostly visible in the logarithmic scale of the df-images.

In previous publications we have described the numerical reconstruction process of df-DHM. In essence, we apply a 2D Fourier Transform (FT) to the detected image and assume an infinite plane wave reference beam. As shown in Fig. 1(b) we obtain the spatial frequency spectrum in k-space where we select the cross-correlation terms that describe the interference between the object and reference beam. Then we select the proper sideband with a computational aperture stop that is centered around the sideband and we shift this sideband to the origin of the k-space. Applying an inverse FFT finally yields the complex image field.

Using the plane wave propagation model for a single-lens imaging system as described by Goodman in [13] we can show that the complex field E_i in image plane is given by [12]:

$$E_i(x_i, y_i) = e^{j\frac{\pi}{\lambda(d_i-f)}(x_i^2+y_i^2)} \left(E_o \left(-\frac{x_i}{M}, -\frac{y_i}{M} \right) \otimes H(x_i, y_i) \right), \quad (1)$$

where $E_o(-\frac{x_i}{M}, -\frac{y_i}{M})$ is the complex field in the object plane and M is the magnification. The quadratic phase term in Eq. (1) has a radius of curvature $d_i - f$ where d_i is the image distance and f is the focal length of the lens. \otimes denotes a convolution and $H(x_i, y_i)$ is the Fourier transform of the aperture stop in the back focal plane of the lens. H is the coherent transfer function (CTF) of this single-lens imaging system and is the Fourier transform of the aperture stop A , given by:

$$H_i(x_i, y_i) = \iint_{-\infty}^{\infty} A(x_f, y_f) e^{-j\frac{2\pi}{\lambda(d_i-f)}(x_f x_i + y_f y_i)} dx_f dy_f. \quad (2)$$

This filtering procedure implicitly assumes that the Fourier transform is zero everywhere outside the sampled region. This is not the case for finite objects. Setting this null space to zero is a simple and convenient solution, however, the procedure corresponds to a multiplication of the true object's Fourier transform with a hard-stop in image space, which in our case is a circle. This results in a convolution of the true object with the Airy function which adds coherent artifacts in our retrieved images that we plan to solve with digital pupil apodization.

2.2. Digital pupil apodization

To correct for these coherent imaging effects a manipulation of the pupil image is required. Earlier we mentioned the multiplexing holograms methods and the image processing methods. With df-DHM we can explore all known methods for noise suppression, but we will focus on the use of window functions during the reconstruction process.

With apodization we can either apodize the hologram in the image plane [25] or in the pupil plane [26] to mainly reduce the diffraction during the numerical reconstruction. Apodization functions can suppress the side lobes of the Airy disk which effectively suppresses ringing effects at object edges at the expense of some loss in resolution. For our investigation we will use cosine-sum window functions that will moderate the effect of the CTF and reduce crosstalk noise by smoothing the higher frequencies of the measured holograms.

The selection of these windows came after the justification made already back in the 70s by Fredric J. Harris [27]. In his work, Harris categorized the numerous window functions based on their significant use and distinct parameters. Starting from the classical rectangle (or Dirichlet) and triangle (or Bartlet) windows, he concluded that windows that are constructed with 3 or 4 nonzero terms (or Dirichlet kernels) can be used for side-lobe suppression.

In this work, we will focus on these window functions as the coefficients are easy to generate and of being able to be applied as a spectral convolution after the 2D DFT. Blackman and the Blackman-Harris windows that are constructed as the summation of 3 and 4 shifted Dirichlet kernels respectively. These window functions are zero-valued outside of a chosen interval, normally symmetric around the middle of the interval, usually near a maximum in the middle, and tapering away from the middle. For our investigation we assume an amplitude apodization

that varies in the radial direction in the pupil plane according to the following cosine-series:

$$\text{win}(\rho) = \sum_{n=0}^N \alpha_n \cos(\pi n \rho), \quad (3)$$

where n are integers of the 2D sum of cosine windows and α_n are the window coefficients which are constrained to a sum of unity. In the simplest case of a rectangular window ($\text{win}(\rho) = 1$) only the first coefficient $\alpha_0 = 1$ is needed, thus a cosine function. To apply this equation to our measured holograms, ρ is the normalized radial position in the pupil plane and is equal to:

$$\rho = \frac{1}{|\vec{k}|} \sqrt{k_x^2 + k_y^2}, \quad (4)$$

k_x, k_y are the k space coordinates that can take values up to the edge of the pupil where we have the maximum spatial frequency of $\text{NA}_{\text{obj}}/\lambda$. Here λ is the wavelength and NA_{obj} is the numerical aperture of the imaging lens ($\text{NA}_{\text{obj}} = 0.5$). We set the size of the apodization window less or equal to NA_{obj} or the boundaries of the cross-correlation term in which we apply the apodization window.

Instead of digital apodization it is also possible to use moving sub-apertures for reducing coherent imaging effects. Similar to the classical physical manipulation of the pupil [28], we can digitally select a smaller window size and apply it on different parts of the pupil image [29]. At the end we take the summation of the intensities of the different reconstructed windows and obtain a noise suppressed df-image. This approach requires multiple holographic reconstructions and thus more time even if it is single shot, and since we need to have a fast numerical reconstruction we will limit our investigation to the use of a single apodized window function in the pupil.

Figure 3 shows the suppression of the side lobes of the PSF for various pupil apodization windows. A first comparison of the different window functions shows that there is a trade-off between width of the side lobe, which determines the resolution, and the suppression of the side lobes, which determines optical crosstalk between neighbouring structures in an image.

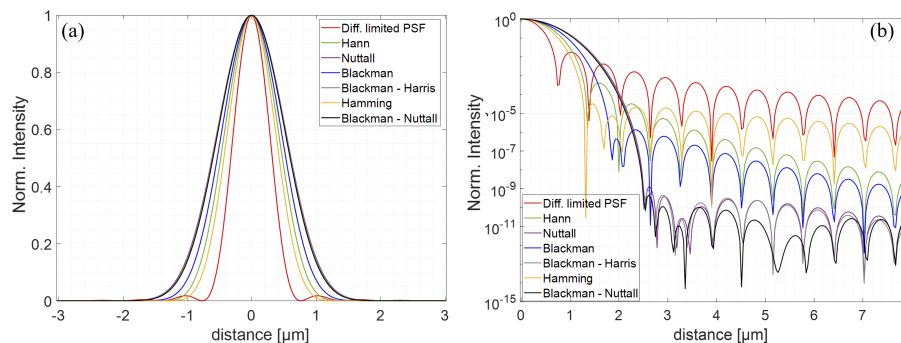


Fig. 3. Theoretical influence of apodization window functions on an ideal PSF. A cross section of normalized intensity image, (a) linear scale, (b) logarithmic scale.

The simulated window functions show that in practice if resolution is not a critical requirement and the application is focused on the coherent effect suppression, the best window functions are the hybrid Blackman windows, and especially the Blackman-Harris, the Blackman-Nuttall and the Nuttall window. On the contrary, if the resolution is important Hamming and Hann windows offer sufficient resolution with less noise suppression. In literature different hybrid window functions have been reported [30] in search for the optimum window that offers almost diffraction

limited resolution with maximum noise suppression. In this work we will focus on the Blackman window as it offers sufficient resolution and suppresses the noise to the required noise levels for metrology.

In [12] we presented an aberration calibration procedure in which we retrieve the wavefront error of our imaging system by measuring the PSF using a point scatterer. Then we only needed to include an aberration correction step on our filtering procedure and obtain an aberration-corrected hologram. We corrected for lens aberrations by multiplying the complex field in the pupil plane with the phase conjugate of the retrieved wavefront error. With the same reasoning we will also perform apodization digitally in the pupil image. This removes the sharp cut-off of the spatial frequency spectrum in the pupil plane resulting in a strong suppression of the side lobes of the PSF. This will suppress optical crosstalk from neighbouring structures that surround a metrology target. The lens aberration correction and the implementation of the window function are then given by:

$$E_{f_{\text{apo}}}(x_f, y_f) = E_f(x_f, y_f)e^{-jW(x_f, y_f)}\text{win}(x_f, y_f). \quad (5)$$

where $E_{f_{\text{apo}}}(x_f, y_f)$ is the corrected field in the exit pupil. In the following section, we apply this concept to both simulations and measurements of PSFs obtained with our df-DHM.

3. Experimental results on coherent imaging effects suppression

3.1. Measurements and simulations on PSF

To investigate the effect of digital apodization on the coherent image quality of metrology targets we start with the characterization of the diffraction-limited point-spread function (PSF). The PSF is the usual way to characterize an optical imaging system, and the proper way to demonstrate the effect of apodization through the side-lobes suppression and the loss of resolution. A point source illuminates the lens aperture with a spherical wave that is insensitive to non-uniformity in the illumination beam. For the measurement we used a bare silicon sample with drilled nano-holes in different parts of the sample. These nano-hole were milled with a 30 keV focused gallium ion beam (FEI Helios Nanolab 600). The ion beam current was set to 100 pA with a focal spot diameter of 80 nm. The nano-holes were milled in 500 cycles and with a dwell time of 1 ms. The diameter of the nano-holes is approximately 80 nm.

The point scatterer was placed in the center of the image field of our DHM setup. Aberration correction was applied to the PSF by applying a wavefront correction to the field in the exit pupil of the lens. The wavefront correction was derived from a Zernike fit of the measured wavefront using the lowest 83 Zernike polynomials. In this way the PSF is only affected by the small residual wavefront errors that could not be captured by the Zernike fit.

For the simulations of the PSF we used the same wavelength, bandwidth and Field of view as the ones that we used for the measurements so that we will have a good comparison between the measurements and the simulations. For the comparison of Fig. 4 we selected a 576 nm wavelength with a bandwidth of 5 nm. At the same time we have included additional shot noise and read-out noise for a better representation of actual measurement conditions. The comparison of simulated and measured PSFs is presented in Fig. 4

From this comparison we observe that the measured unapodized PSF and the PSF after apodization with a Blackman window could not surpass a noise floor of the order of 10^{-6} (or -60 dB), as shown in Fig. 4(e). On the other hand, we observe that the simulated PSFs show excellent sidelobe suppression after apodization. At a closer look to the center of the Airy disk and the apodized PSF, we see that there is a good correlation between the simulations and the measurements, Fig. 4(f). At this point and for noise levels above 10^{-5} we see that the simulated and the measured diffraction-limited PSFs are overlapping while in the contrary the apodization windows reach this noise level immediately after the 1st Airy ring.

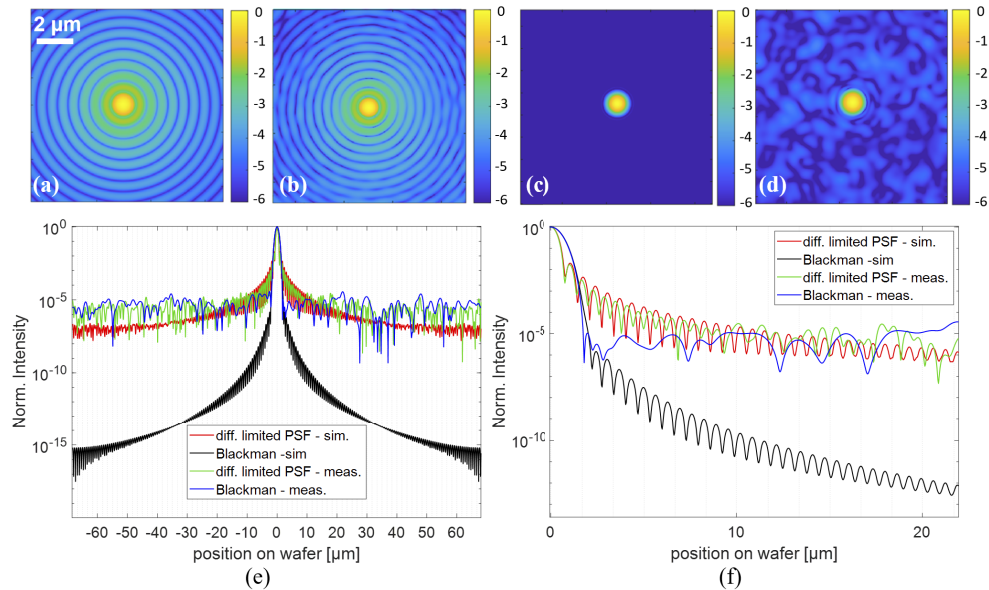


Fig. 4. Comparison of simulated and measured PSFs. (a) simulated Airy disk, (b) measured Airy disk, (c) simulated apodization with Blackman window, (d) measured apodization with Blackman window. (e) presents the cross-section of the above images in logarithmic scale, and (f) provides a closer look on the response in the 4 different cases.

The flattening of the noise shows that the use of apodization windows does not offer sufficient coherent imaging effects suppression in our DHM setup. In that sense while apodization can assist with the crosstalk reduction and reduction of the ringing effects in the region-of-interest in the metrology target area, it will still lead to a noise suppression at 10^{-5} noise levels. In the next section, we will present the experimental data from which we were able to locate the cause of the observed noise floor.

3.2. Effectiveness of apodization and potential limitations

In order to investigate the cause of the noise flattening on the experimental data we look into three potential noise sources that could contribute to this effect:

1. Roughness of the silicon wafer
2. Detection noise
3. Scattering from lens imperfections

3.2.1. Roughness of the silicon wafer

Starting with the roughness of the silicon wafer, an atomic force microscopy scan of the roughness showed a root-mean-square (RMS) error of 142 pm and maximum peak-to-valley of 2.3 nm during the scan. These values suggest that the sample was very smooth and is probably not introducing speckle to our measurements. A simple method to check the presence of speckle coming from the wafer is to compare the high-frequency residual wavefront variations in the exit pupil of our imaging lens for different nano-holes. If the roughness of the silicon dominates the noise floor that is shown in Fig. 4 then this should show up as noise in the wavefront residual in the exit pupil. The fingerprint of this noise in the wavefront residual should then vary between

different nano-hole measurements. In other words, the wavefront residuals measured for two nanoholes should show little or no correlation.

To experimentally test this hypothesis we have selected two nano-holes with approximately the same size (measured with AFM). For these 2 nano-holes we measured the WFE (Fig. 5(a) and 5(d)) in the pupil and we subtracted a fitted wavefront (using the lowest 83 Zernike polynomials). The resulting residual WFEs of the 2 nano-holes show high-frequency variations that are shown in Fig. 5(c) and 5(f). The two locations have a clear speckle correlation which suggests that surface roughness of the silicon substrate does not contribute significantly to the high-frequency speckle-like wavefront variations. The measured correlation was 0.8130 with a deviation that can be contributed to additional noise on the second PSF. As shown in Fig. 5(d), there is a phase gradient present in the measured WFE, which is attributed to a nearby nano-hole that introduced additional scattering to the measured wavefront.

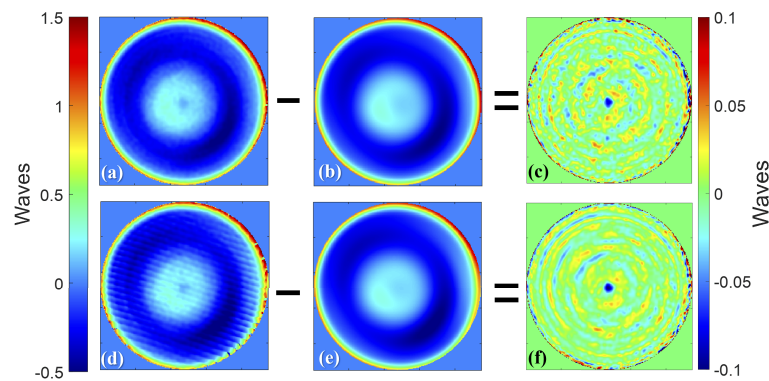


Fig. 5. Residual wavefront errors for two PSFs. (a), (d) are the measured WFEs and (b),(e) are the fitted aberration terms. (c) and (f) presents the residual wavefront errors for the two PSFs simply by removing the fitted wavefronts from the measured ones.

3.2.2. Impact of detection noise

The detected digital hologram contains shot noise that is inherent to the detection of photons. Moreover, the image sensor also adds some read noise to this shot noise. In order to test the impact of these noise sources we performed a frame averaging on the same PSF.

Figure 6 presents a comparison of the measured PSF in a single holographic reconstruction and after 150x reconstructions. It is clear that after frame averaging there is no improvement with respect to the noise levels, meaning that our measurements are not limited by shot noise and image sensor read noise. In principle, in holography this is expected due to coherent amplification. Even if the object beam is weak, in our case the PSF, it is coherently amplified by the reference beam.

3.2.3. Scattering from lens imperfections

Our df-DHM uses an off-the-shelf plano-aspheric lens (Thorlabs A240TM) with an effective focal length of 8 mm and an NA of 0.5. Because of the extreme level of aberrations on the edges of the used lens, we have selected a digital aperture stop of 0.48. According to the data supplied by Thorlabs, we should expect a root-mean-square (RMS) wavefront error (WFE) of 0.058 waves. As a result of this residual wavefront error, some weak scattering will occur at the lens surfaces which results in a weak speckle background in the retrieved images.

A simple method to check the presence of lens-induced light scattering is to look at high-frequency residual wavefront variations in the exit pupil of our Thorlabs A240TM imaging lens.

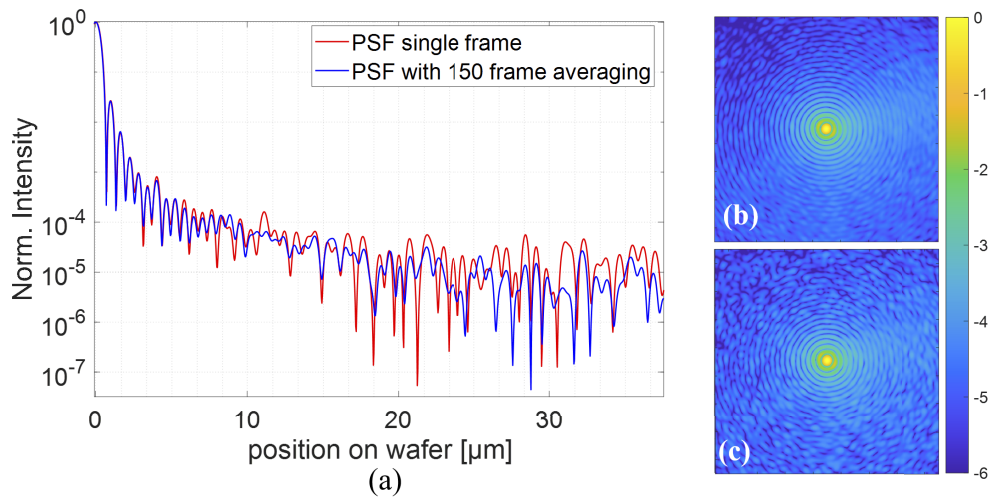


Fig. 6. (a) Cross-section of the normalized intensity of a PSF measured with and without frame averaging. (b) and (c) The single-frame measured PSF and the same PSF after 150 frames averaging. Both figures presented in logarithmic scale.

Similarly to what we presented in Fig. 5, in the case of scattering from the lens, we will measure the same PSF for three different wavelengths. As a result of the close proximity of the exit pupil to the lens this residual WFE will be more or less invariant for small wavelength changes.

To measure this correlation we retrieved the complex WFE for three closely spaced wavelengths (532, 550 and 576 nm) and then removed a fitted wavefront that we obtained by fitting the lowest 83 Zernike polynomials to the measured wavefront. We can then measure the residual phase variation in the pupil. If the residual phase variation or the residual WFE of the PSF show significant correlation for different wavelengths then this is another indication that light scattering from the lens is the main cause of the observed speckle.

Figure 7, presents the residual wavefront errors that we obtained by measuring the PSF at three different wavelengths. For every wavelength (532, 550 and 576 nm) we remove the fitted aberrations terms from the retrieved WFE and we plot the residual WFE. As shown all graphs show a clear correlation of the residual WFE which is a very strong indication that our measurements are impacted by the roughness of the lens surface. To measure the correlation coefficient for different wavelengths we had to resize the measured WFE as the size of the sideband in the angular spectrum is wavelength dependent (Eq. (5)). We resize the WFE with respect to the middle wavelength and we measured correlations above 0.75. In details, the correlation between 7.(a) and 7.(b) was 0.7678, between 7.(a) and 7.(c) was 0.8018 and between 7.(b) and 7.(c) 0.7805.

Moreover, we computed the RMS error for the three wavelengths and it was 0.0510, 0.0560, and 0.0516 waves respectively which is close to the expected wavefront error that has been specified by the supplier of this lens. This is another clear indication that scattering caused by the lens is the main cause for the speckle background that we observe in our images.

For the three wavelengths there is some additional noise present in the edges of the pupil which is more visible on the shorter wavelengths and on the right side. This additional WFE could be related to the size of the aperture stop in the pupil which we considered fixed for an NA of 0.48 or it can be an error during the filtering of the holographic process that we neglected for the time being.

In order to further substantiate our observation we performed a second experiment where we replaced the sample with the tip of a single-mode fiber. We used a polarization maintaining

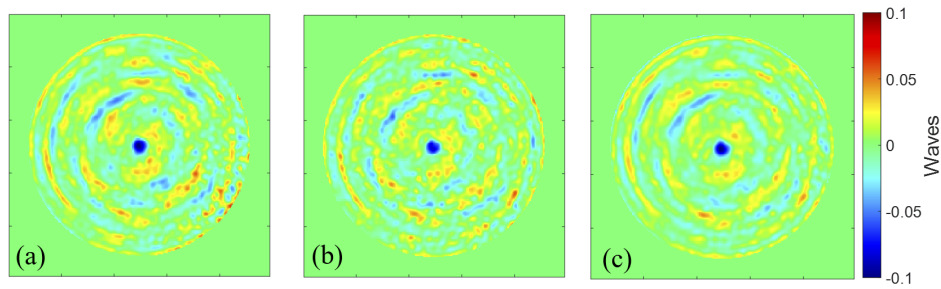


Fig. 7. Lens surface roughness. Residual Wavefront Error experiment. (a), (b), (c) the RWE for the measured PSF for 532, 550 and 576 nm wavelength respectively.

PANDA fiber (Schafter Kirchhof – PMC-E-400Si-3.5-NA013-3-APC.EC-150-P) with nominal NA of 0.13 and a mode field diameter (MFD) of $3.5\ \mu\text{m}$. The use of a fiber tip to measure the PSF has already been reported by [31] and it allows us to exclude the impact of any scattering from the silicon substrate that we used for the previous experiments. However in our experiment due to the small NA of the fiber, which at a 520–580 nm wavelength range is ≈ 0.08 , instead of an Airy disk, df-DHM will image a Gaussian spot.

For the measurements with the fiber tip we selected three different wavelengths (532, 550, and 576 nm) and we look into the speckle correlation on the reconstructed images. Figure 8 summarize the measurements with the fiber tip. Figure 8(a), (b), and (c) show the normalized intensity images of the holographically reconstructed Gaussian spot of the fiber tip for the three selected wavelengths in logarithmic scale. For these measurements we have averaged 100x reconstructed images.

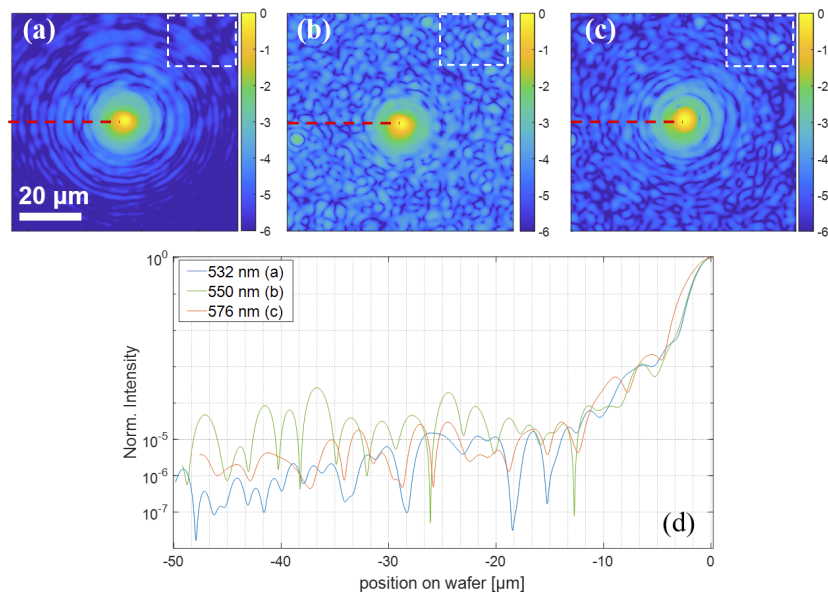


Fig. 8. Fiber-tip experiment. (a),(b) and (c) are the holographically reconstructed intensity images of the fiber tip for 532, 550 and 576 nm wavelength respectively. (d) Logarithmic plot of the cross-section (as indicated with the red dotted line) of the normalized intensities of the measured Gaussian spots.

A cross-section plot of the measured normalized intensity in Fig. 8(d) shows that for all the wavelengths the noise levels are of the same order. Looking at the speckle correlation between different wavelengths, it is clear that there is no correlation between the three measurements. To confirm that we have also measured the correlation coefficients between (a), (b), and (c) within the drawn squares and the correlation was below 10%. The absence of correlation between the three measured signals again points to lens scattering as the main suspect for the observed speckle in our images.

At this point, it is good to highlight that the speckle that we measured with DHM was impossible to detect with regular imaging of the fiber-tip. We have performed the same measurements without additional reference beams and look into the measured normalized intensities of the 3 different wavelengths after averaging 100 images. Figure 9(a), (b), and (c) show the normalized intensity images of the Gaussian spot of the fiber tip for the three selected wavelengths in logarithmic scale. A cross-section plot of the measured normalized intensity in Fig. 9(d) confirms that in regular imaging the measurements are buried in the read out noise and corresponds to a lower noise suppression, making it impossible to detect speckle. This clearly shows the superior dynamic range capabilities of DHM compared to regular imaging techniques.

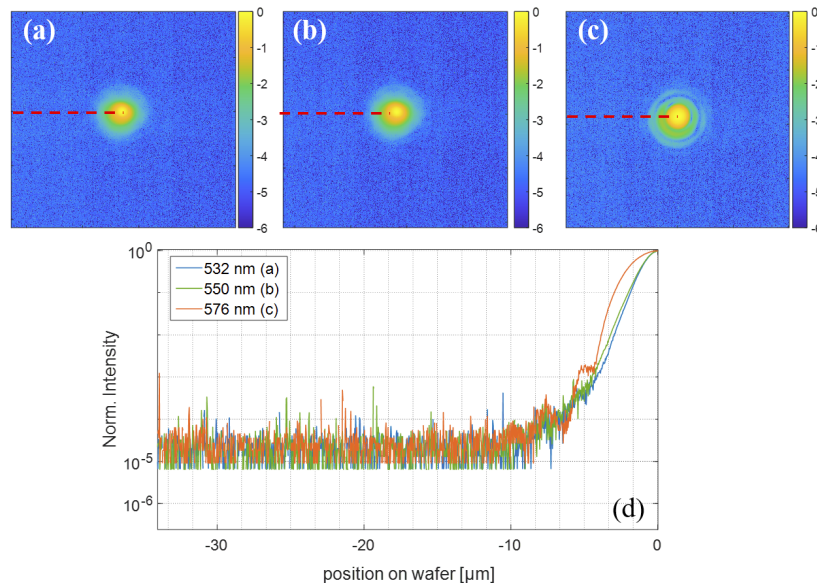


Fig. 9. Fiber-tip experiment. (a), (b) and (c) are the normalized intensity images of the fiber tip for 532, 550 and 576 nm wavelength respectively. (d) Logarithmic plot of the cross-section (as indicated with the red dotted line) of the normalized intensities of the measured Gaussian spots.

In the next subsection, we apply digital apodization on actual metrology targets. We will show that even with the presence of micro-speckle from the lens roughness apodization can still contribute to df-DHM by suppressing a large part of coherent imaging artifacts.

3.3. Measurements and simulations on metrology targets

Since we quantify the digital apodization response to a PSF, now we will apply apodization windows to metrology targets to see the response on coherent imaging effects suppression on measured holograms. We selected a micro-DBO (μ DBO) metrology target with $8 \times 8 \mu\text{m}^2$ feature size that consists of four grating pairs with a grating pitch of 600 nm, like the one shown in Fig. 2.

We will first simulate the effect of apodization neglecting the effect of micro-speckle of the lens surface. With these simulations we can estimate the effectiveness of digital apodization on metrology targets on ideal conditions. Then we will present actual measurements where we will apply the same apodization window to see the coherent imaging effect suppression on the current setup. For both simulations and measurements we will use same setup parameters, with an NA of 0.48 and a selected wavelength of 576 nm.

For the simulations the same targets were simulated and the Blackman apodization window was applied. The results of the simulations are shown in Fig. 10. Figure 10(a) and 10(b) show the simulated target on a regular image and an image where the Blackman window was applied on the pupil plane. Figure 10(c) presents the cross section in logarithmic scale where the effectiveness of apodization is impressive. We can see at least a 10^{-5} coherent noise suppression and a smooth surface for the metrology mark, with no coherent artifacts present.

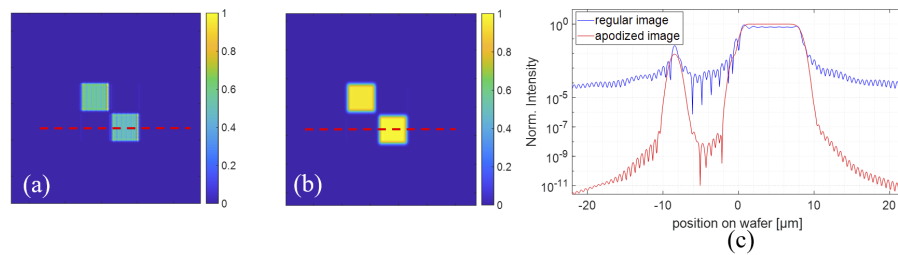


Fig. 10. Simulated results of digital apodization on metrology targets. (a) a regular image obtained after holographic reconstruction, (b) apodized image with Blackman apodization window. (c) is the cross-section along the red-dashed lines, where blue and red lines show the normalized intensity of the regular and apodized image respectively.

For the measurements of this metrology target we first correct for lens aberrations, in order to obtain an aberration free "regular" image and then we applied the Blackman window in the pupil plane. Figure 11 shows the effect of apodization on the metrology target on the current df-DHM setup. In the measurements we see that the intensity smoothens on the surface of the metrology target and completely suppresses Gibbs artifacts. At the same time multiple spurious oscillations on the surrounding area are also suppressed by an order of magnitude. This is still far from the ideal result that was presented on the simulations but it already convincingly shows a fast way to remove coherent imaging effects by applying a digital apodization in the pupil plane.

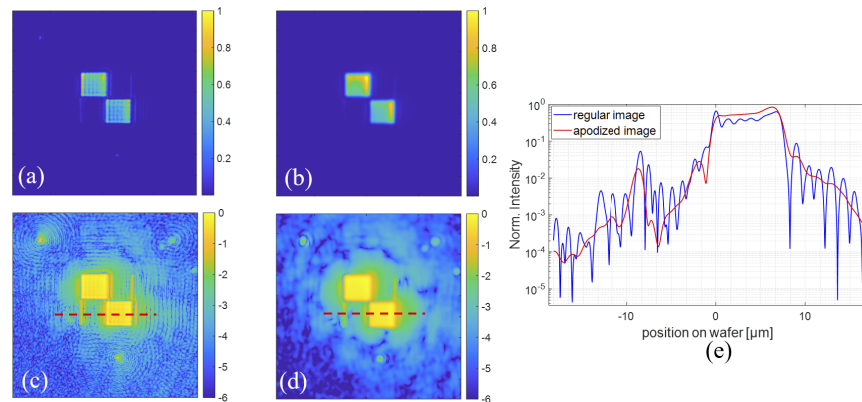


Fig. 11. Experimental results of digital apodization on metrology targets. (a) a regular image obtained after holographic reconstruction, (b) apodized image with Blackman apodization window. (c), (d) regular and apodized image in logarithmic scale. (e) is the cross-section along the red-dashed lines, where blue and red lines show the normalized intensity of the regular and apodized image respectively.

4. Conclusion

We have investigated the potential of digital pupil apodization in DHM for coherent imaging effect suppression. We presented both simulations and measurements that demonstrate the simplicity of this method where a 2D window function needs to be included in the holographic reconstruction.

We have first applied apodization to diffraction limited PSF's ("Airy disks") to demonstrate the effectiveness on side lobe suppression. The results showed that apodization clearly suppresses side lobes of the Airy disc. This side lobe suppression helps to reduce optical crosstalk between images of neighbouring structures at the expense of some resolution loss. This is especially relevant in optical wafer metrology applications like overlay metrology where a small metrology target is often surrounded by other patterns. Light from these surrounding patterns that "leak" into the metrology target resulting in a reduced metrology performance.

During our investigation we observed the presence of a weak background speckle in our PSF images that limited the effectiveness of apodization. By conducting a number of experiments we identified that the quality of the lens surface is the main factor of this deviation. The lens surface roughness adds micro-speckle on the measurements which in extend create a noise barrier that prevents apodization to reach its full potential. The lens that we currently use is an off-the-shelf low-cost glass-moulded lens. We expect that more advanced lens manufacturing techniques will allow us to significantly reduce the noise floor that we now observe in our results.

However, the size of the window function can proven to be beneficial on higher diffraction order suppression. For example, in an overlay measurement where we look on the intensity imbalance between the +1st and -1st diffraction order images there might be an overlap with a higher diffraction order in the image plane. This can be easily removed by carefully placing the window function in a smaller aperture size centered around the 1st diffraction order in the pupil. This leaves the main frequency contributions of the higher order out of the reconstructed image.

This work has shown that df-DHM has the potential to be a powerful tool in optical wafer metrology provided that we can suppress the lens-induced light scattering to sufficiently low levels. Current measurements still show relatively large background noise levels, we plan to continue this investigation with a better lens quality which we are confident that will lead to robust coherent imaging effect suppression. This work also highlighted the excellent dynamic range of DHM compared to typical microscopy measurements. DHM was sensitive to the effect of lens

roughness while a typical intensity image was buried in camera noise, unable to demonstrate this effect.

Funding. ASML; Advanced Research Center for Nanolithography; Vrije Universiteit Amsterdam.

Acknowledgements. We gratefully acknowledge the valuable suggestion from Hugo Cramer, Senior Researcher at ASML, on the measurement of the speckle correlation in the pupil plane of our imaging lens. We would like to thank Vasco Tenner, Optical Researcher at ASML, and Marco Konijnenburg, Head Software Engineering group of AMOLF/ARCNL for their support and contribution to this project.

Disclosures. The authors declare no conflicts of interest. The authors declare that they have patents or patent applications. The authors Theodorus T. M. van Schaijk and Arie den Boef are employees of ASML.

Data availability. Data underlying the results presented in this paper are not publicly available at this time but may be obtained from the authors upon reasonable request.

References

1. M. K. Kim, "Principles and techniques of digital holographic microscopy," *J. Photon. Energy* **1**(1), 018005 (2010).
2. W. Osten, A. Faridian, P. Gao, K. Körner, D. Naik, G. Pedrini, A. K. Singh, M. Takeda, and M. Wilke, "Recent advances in digital holography," *Appl. Opt.* **53**(27), G44–G63 (2014).
3. T. Tahara, X. Quan, R. Otani, Y. Takaki, and O. Matoba, "Digital holography and its multidimensional imaging applications: a review," *Microscopy* **67**(2), 55–67 (2018).
4. M. A. Schulze, M. A. Hunt, E. Voelkl, J. D. Hickson, W. R. Usry, R. G. Smith, and R. Bryant and C. E. T. Jr., "Semiconductor wafer defect detection using digital holography," in *Process and Materials Characterization and Diagnostics in IC Manufacturing*, vol. 5041 K. W. T. Jr. and I. Emami, eds., International Society for Optics and Photonics (SPIE, 2003), pp. 183–193.
5. A. Stadelmaier and J. H. Massig, "Compensation of lens aberrations in digital holography," *Opt. Lett.* **25**(22), 1630–1632 (2000).
6. Y. Liu, Z. Wang, and J. Huang, "Recent progress on aberration compensation and coherent noise suppression in digital holography," *Appl. Sci.* **8**(3), 444 (2018).
7. C. Messinis, T. T. M. van Schaijk, N. Pandey, V. T. Tenner, S. Witte, J. F. de Boer, and A. den Boef, "Diffraction-based overlay metrology using angular-multiplexed acquisition of dark-field digital holograms," *Opt. Express* **28**(25), 37419–37435 (2020).
8. T. T. M. van Schaijk, C. Messinis, N. Pandey, A. Koolen, S. Witte, J. F. de Boer, and A. den Boef, "Diffraction-based overlay metrology from visible to infrared wavelengths using a single sensor," *J. Micro/Nanopattern. Mats. Metro.* **21**(1), 014001 (2022).
9. A. J. den Boef, "Optical wafer metrology sensors for process-robust cd and overlay control in semiconductor device manufacturing," *Surf. Topogr.: Metrol. Prop.* **4**, 023001 (2016).
10. J. Kim, J. Lee, C. Hwang, S. Y. Lee, W. Jung, J. Park, K. Bhattacharyya, A. den Boef, S. Mathijssen, M. Noot, F. Farhadzadeh, D. Park, K. Padhye, S.-R. Jeon, S.-B. Yang, W.-J. Jang, and O.-S. Kwon, "Taking the multi-wavelength DBO to the next level of accuracy and robustness," in *Metrology, Inspection, and Process Control for Microlithography XXXIV*, vol. 11325 O. Adan and J. C. Robinson, eds., International Society for Optics and Photonics (SPIE, 2020), pp. 222–227.
11. G. E. Moore, "Cramming more components onto integrated circuits, reprinted from electronics, volume 38, number 8, april 19, 1965, pp. 114 ff.," *IEEE Solid-State Circuits Soc. Newsl.* **11**(3), 33–35 (2006).
12. C. Messinis, T. T. M. van Schaijk, N. Pandey, A. Koolen, I. Shlesinger, X. Liu, S. Witte, J. F. de Boer, and A. den Boef, "Aberration calibration and correction with nano-scatterers in digital holographic microscopy for semiconductor metrology," *Opt. Express* **29**(23), 38237–38256 (2021).
13. J. W. Goodman, *Introduction to Fourier optics*, 4th ed. (W.H. Freeman and Co., 2017), chap. 4-6, pp. 75–166.
14. J. Garcia-Sucerquia, "Noise reduction in digital lensless holographic microscopy by engineering the light from a light-emitting diode," *Appl. Opt.* **52**(1), A232–A239 (2013).
15. F. Dubois, L. Joannes, and J.-C. Legros, "Improved three-dimensional imaging with a digital holography microscope with a source of partial spatial coherence," *Appl. Opt.* **38**(34), 7085–7094 (1999).
16. J. Dohet-Eraly, C. Yourassowsky, A. E. Mallahi, and F. Dubois, "Quantitative assessment of noise reduction with partial spatial coherence illumination in digital holographic microscopy," *Opt. Lett.* **41**(1), 111–114 (2016).
17. F. Pan, W. Xiao, S. Liu, F. Wang, L. Rong, and R. Li, "Coherent noise reduction in digital holographic phase contrast microscopy by slightly shifting object," *Opt. Express* **19**(5), 3862–3869 (2011).
18. Y. Wang, P. Meng, D. Wang, L. Rong, and S. Panzai, "Speckle noise suppression in digital holography by angular diversity with phase-only spatial light modulator," *Opt. Express* **21**(17), 19568–19578 (2013).
19. S. Shin, K. Kim, K. Lee, S. Lee, and Y. Park, "Effects of spatiotemporal coherence on interferometric microscopy," *Opt. Express* **25**(7), 8085–8097 (2017).
20. A. Sharma, G. Sheoran, Z. Jaffery, and Moinuddin, "Improvement of signal-to-noise ratio in digital holography using wavelet transform," *Opt. Lasers Eng.* **46**(1), 42–47 (2008).
21. V. Bianco, M. Paturzo, P. Memmolo, A. Finizio, P. Ferraro, and B. Javidi, "Random resampling masks: a non-bayesian one-shot strategy for noise reduction in digital holography," *Opt. Lett.* **38**(5), 619–621 (2013).

22. M. Haouat, J. Garcia-Sucerquia, A. Kellou, and P. Picart, "Reduction of speckle noise in holographic images using spatial jittering in numerical reconstructions," *Opt. Lett.* **42**(6), 1047–1050 (2017).
23. F. Pan, L. Yang, and W. Xiao, "Coherent noise reduction in digital holographic microscopy by averaging multiple holograms recorded with a multimode laser," *Opt. Express* **25**(18), 21815–21825 (2017).
24. X. Zhao, H. Zhang, Y. Zhou, W. Bian, T. Zhang, and X. Zou, "Gibbs-ringing artifact suppression with knowledge transfer from natural images to mr images," *Multimedia Tools Appl.* **79**(45-46), 33711–33733 (2020).
25. E. Cucho, P. Marquet, and C. Depeursinge, "Aperture apodization using cubic spline interpolation: application in digital holographic microscopy," *Opt. Commun.* **182**(1-3), 59–69 (2000).
26. C. H. Seo and J. T. Yen, "Sidelobe suppression in ultrasound imaging using dual apodization with cross-correlation," *IEEE Trans. Ultrason., Ferroelect., Freq. Contr.* **55**(10), 2198–2210 (2008).
27. F. Harris, "On the use of windows for harmonic analysis with the discrete fourier transform," *Proc. IEEE* **66**(1), 51–83 (1978).
28. C. Buitrago-Duque and J. Garcia-Sucerquia, "Physical pupil manipulation for speckle reduction in digital holographic microscopy," *Heliyon* **7**(1), e06098 (2021).
29. D. Hincapie, J. Herrera-Ramírez, and J. Garcia-Sucerquia, "Single-shot speckle reduction in numerical reconstruction of digitally recorded holograms," *Opt. Lett.* **40**(8), 1623–1626 (2015).
30. N. A. Mohammed, T. A. Ali, and M. H. Aly, "Performance optimization of apodized FBG-based temperature sensors in single and quasi-distributed DWDM systems with new and different apodization profiles," *AIP Adv.* **3**(12), 122125 (2013).
31. F. Charrière, A. Marian, T. stan Colomb, P. Marquet, and C. Depeursinge, "Amplitude point-spread function measurement of high-na microscope objectives by digital holographic microscopy," *Opt. Lett.* **32**(16), 2456–2458 (2007).